

News from Gaia on σ Ori E: a case study for the wind magnetic braking process

H.F. Song¹, G. Meynet^{2,†}, A. Maeder², N. Mowlavi², S.R. Stroud², Z. Keszthelyi³, S. Ekström², P. Eggenberger², C. Georgy², G. A. Wade⁴, Y. Qin^{5,6}

¹ College of Physics, Guizhou University, Guiyang city, Guizhou Province, 550025, P.R. China

² Geneva Observatory, Geneva University, CH-1290 Sauverny, Switzerland

³ Anton Pannekoek Institute for Astronomy, University of Amsterdam, Science Park 904, 1098 XH, Amsterdam, The Netherlands

⁴ Department of Physics and Space Science, Royal Military College of Canada, PO Box 17000, Station Forces, Kingston, Ontario, Canada, K7K7B4

⁵ Department of Physics, Anhui Normal University, Wuhu city, Anhui Province, 241000, P.R. China

⁶ Center for Interdisciplinary Exploration and Research in Astrophysics (CIERA) and Department of Physics and Astronomy, Northwestern University, Sherman Avenue, Evanston, IL 60201, USA

[†]Corresponding author, e-mail: georges.meynet@unige.ch

Received; accepted

ABSTRACT

Context. σ Ori E, a massive helium B-type star, shows a high surface rotation and a strong surface magnetic field potentially challenging the process of wind magnetic braking.

Aims. The Gaia satellite provides an accurate distance to that star and confirms its membership to the σ Ori cluster. We account for these two key pieces of information to investigate whether single star models can reproduce the observed properties of σ Ori E and provide new estimates for its metallicity, mass, and age.

Methods. We compute rotating stellar models accounting for wind magnetic braking and magnetic quenching of the mass loss. Two metallicities ($Z=0.014$, with a helium mass fraction $Y=0.273$ and $Z=0.020$ with $Y = 0.266$), four initial masses between 8 and 9 M_{\odot} , three initial rotations between 250 and 450 km s^{-1} and three initial surface equatorial magnetic field between 3 and 7 kG are considered. Differential rotation is assumed for the internal rotation in all models. We look for models accounting simultaneously for the observed radius, position in the HR diagram, surface velocity, and braking timescale.

Results. We obtain that σ Ori E is a very young star (age less than 1 Myr) with an initial mass around 9 M_{\odot} , a surface equatorial magnetic field around 7 kG and having a metallicity Z (mass fraction of heavy elements) around 0.020. No solution is obtained with the present models for a metallicity $Z=0.014$. The initial rotation of the models fitting σ Ori E is not much constrained and can be anywhere in the range studied here. Because of its very young age, models predict no observable changes of the surface abundances due to rotational mixing.

Conclusions. The simultaneous high surface rotation and high surface magnetic field of σ Ori E may simply be a consequence of its young age. This young age implies that the processes responsible for producing the chemical inhomogeneities that are observed at its surface should be rapid. Thus for explaining the properties of σ Ori E, there is no necessity to invoke a merging event although such a scenario cannot be discarded. Other stars (HR 5907, HR 7355, HR 345439, HD 2347, CPD -50°3509) showing similar properties as σ Ori E (fast rotation and strong surface magnetic field) may also be very young stars, although determination of the braking timescales is needed to confirm such a conclusion.

Key words. stars:rotation; stars: abundances; stars: magnetic field; stars:evolution

1. Introduction

The star σ Ori E (HD 37479) is a magnetic, He-strong, Main-Sequence star of spectral type B2Vpe (Osmer & Peterson 1974; Landstreet & Borra 1978). It shows variations of helium abundance across its surface (Krtićka et al. 2020). It has a strong surface magnetic field whose morphology combines a dipolar component, with a polar strength $B_{\text{dip}} = 7.3 - 7.8$ kG with obliquity $47^{\circ} - 59^{\circ}$, and a smaller non-axisymmetric quadrupole component with strength $B_{\text{qua}} = 3 - 5$ kG (Oksala et al. 2015). It has a relatively fast rotation (P_{rot} is equal to 1.19 days, implying, see below, a surface equatorial velocity of ~ 160 km s^{-1} , Townsend et al. 2010).

Direct measurements of rotational period change exist for just four magnetic stars: CU Vir, HD 37776, σ Ori E, and HD

142990. The rotation of σ Ori E is observed to slow down at approximately the rate predicted by analytical prescriptions of magnetic braking (ud-Doula & Owocki 2002; Townsend et al. 2010; Oksala et al. 2012). Interestingly, in the three other cases, apparently cyclical period changes - including episodes of rotational acceleration - have been observed (Mikulášek et al. 2011; Shultz et al. 2019a).

The first measure of period change for σ Ori E was done by Mikulášek et al. (2008). These authors have obtained for the ratio P_{rot}/\dot{P} , where P_{rot} is the rotation period and \dot{P} , the rate of its change, a value of 0.25 Myr. We shall call this ratio the present-day braking timescale. For this ratio, Townsend et al. (2010) gives a value of 1.3 Myr, so considerably longer. Still more recently, Petit et al (in preparation) obtain a value of 1.12

Myr¹. In the present paper, we shall stick to the published value by Townsend et al. (2010). The present braking timescale is not giving an estimate of the age of the star or of the duration of the period during which the star has been braked because we do not know how P_{rot}/\dot{P} evolves. For instance, the braking timescale can be significantly shorter than the age of the star if, for instance, the surface is continuously accelerated by a transport of angular momentum from the core to the envelope, or if the star has been spun up by an interaction or a merging with a companion. The braking timescale can also be larger than the age of the star in case the star would be in a very early phase of its evolution.

In this paper we want to identify what is the most probable status of σ Ori E. Is it a star at a very early stage of its evolution, in which case there will no problem to explain both its strong surface magnetic field and rapid rotation. Is it an evolved star, with a braking timescale shorter than its age? In that case, either some efficient internal transport of angular momentum would be required for single star to reproduce the observed properties or an interaction with a close companion has to be invoked.

If the star σ Ori E belongs to the σ Ori cluster as has been assumed by Townsend et al. (2013), and if the age of this cluster is around 2-3 Myr as given by Sherry et al. (2008) and Caballero (2007), then we would have a configuration where the age of the star is slightly larger than the present braking timescale. If σ Ori E indeed belongs to the σ Ori cluster and the determined age is correct (actually age determinations are very model dependent), we are left with one of the two last possibilities, either a single star with some internal angular momentum transport or a binary with, at a given time, an interaction that has spun up the star (by tides, mass accretion or merging process).

In the present paper, we want first take profit from the Gaia Data Release 2 to obtain a better estimate of the distance of σ Ori E and get some clues about its belonging or not to the σ Ori cluster. As explained below, knowing the distance allows the determination of the radius of the star (thanks to a photometric estimate of the angular diameter). From the observed rotation period and the stellar radius, one can obtain the surface velocity. From the radius and the effective temperature, one can estimate the luminosity of σ Ori E. Adding the observed value of P_{rot}/\dot{P} , this makes five constraints (radius, surface velocity, luminosity, effective temperature and present braking timescale) that any model has to reproduce. The question that we want to address here: do single star models exist able to reproduce these five constraints? If yes, what would be the range of ages for σ Ori E? What would be other, still non observed properties that such models would predict for σ Ori E?

We present in section 2 the observed properties of σ Ori E. The physics of our stellar models is explained in Sect. 3. Section 4 looks for models reproducing the above five observed constraints. The results are discussed in Sect. 5 and the main conclusions are given in Sect. 6.

2. Observational constraints of σ Ori E

2.1. Distance of σ Ori E

Distance estimates for σ Ori E before the *Gaia* data releases relied on the distance to the cluster. This distance ranges in the literature from 352^{+166}_{-168} pc to 473 ± 33 pc (see Table 2 in Caballero

¹ New \dot{P}_{rot} of 91.9 ms per year is measured by Petit et al. (in prep). This gives, considering a rotation period of 1.19 days, a value of the ratio equal to 1.12 Myr.

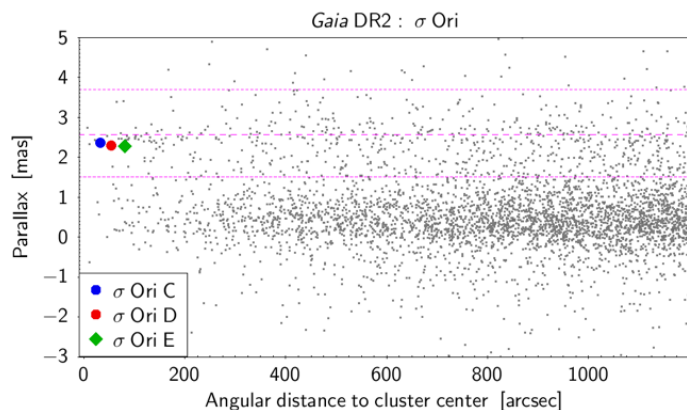


Fig. 1. *Gaia* DR2 parallaxes of all stars in the direction of the σ Ori cluster versus their *Gaia* DR2 distance to the cluster center taken at (RA, Dec) = (84.675, -2.6) deg from Simbad. The dashed and dotted horizontal lines indicate the mean and one standard deviation limits, respectively, of the parallaxes as determined by Caballero (2018) from cluster members. The positions of σ Ori C, D and E in the diagram are indicated by the blue, red filled circles and the green filled diamond, respectively.

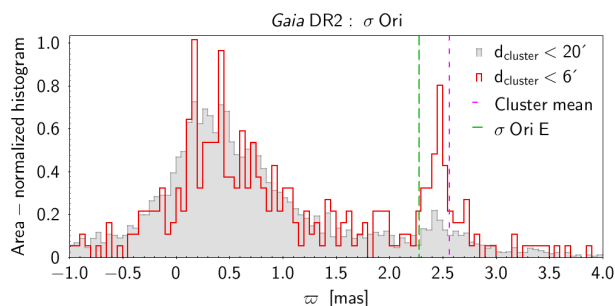


Fig. 2. Histograms of the *Gaia* DR2 parallaxes of all stars within a distance on the sky of 6 arcmin (open red histogram) and 20 arcmin (filled gray histogram) to the cluster center taken at the same position as in Fig. 1. The histograms are area-normalized. The vertical short magenta dashed line locates the mean *Gaia* DR2 parallax of the cluster as determined by Caballero (2018). The vertical long green dashed line locates the *Gaia* DR2 parallax of σ Ori E.

2017). It is only with the parallaxes obtained by *Gaia* that an individual distance to σ Ori E has been provided. We note that no parallax was provided by Hipparcos for this star.

The proper motion of σ Ori E confirms that this star is a member of the young σ Orionis open cluster. Based on a sample of 281 star members including brown dwarfs, Caballero (2018) derive a mean parallax of the cluster from *Gaia* DR2 parallaxes of 2.56 ± 0.29 mas. This corresponds to a mean distance of 391^{+50}_{-40} pc. The cluster is very extended in space, making it unprecise to assume the distance of an individual member to be equal to the distance of the cluster. This is shown in Fig. 1, which plots the *Gaia* DR2 parallaxes versus sky distance of all stars within 30 arcmin from the center of the cluster. The cluster stands out from background stars at parallaxes within the 2.56 ± 0.29 mas limits, shown by the magenta dotted lines in the figure. It is even more clearly seen in Fig. 2, which plots in red the histogram of the parallaxes of stars within 6 arcmin from the cluster center against the histogram in filled gray of stars within 20 arcmin from the cluster center.

The three bright stars σ Ori C, D and E are highlighted in Fig. 1 with colored filled circles. They are close to the center of the cluster and have parallaxes smaller than the mean of the

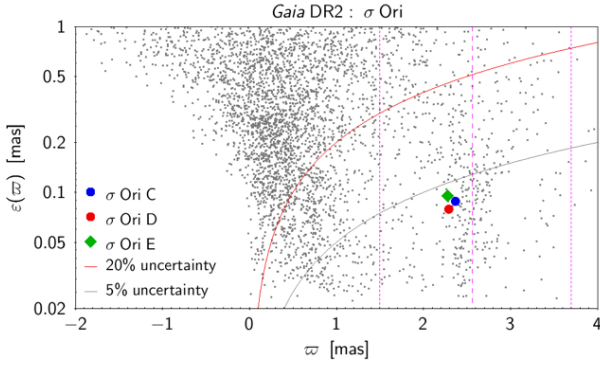


Fig. 3. *Gaia* DR2 parallax uncertainties versus parallax of all stars within a distance on the sky of 20 arcmin to the cluster center taken at the same position as in Fig. 1. The dashed and dotted vertical lines indicate the mean and one standard deviation limits, respectively, of the parallaxes as determined by Caballero (2018) from cluster members. The red and gray solid lines indicate the parallax uncertainty limit at any given parallax below which the relative uncertainty is less than 20% and 5%, respectively. The positions of σ Ori C, D and E in the diagram are indicated by the blue, red filled circles and the green filled diamond, respectively.

Table 1. Observational data on σ Ori E

Gaia Astrometry		
Distance	439^{+20}_{-19} pc	Gaia Collaboration et al. (2018)
Spectropolarimetry		
Polar magnetic field, B_p	7.3-7.8 kG	Oksala et al. (2012, 2015) Townsend et al. (2010, 2013)
$\log g$	4.0 ± 0.5	Oksala et al. (2012, 2015)
Photometry		
Rotational period, P_{rot}	1.19 days	Townsend et al. (2010, 2013)
\dot{P}_{rot}	77 mms per year	Townsend et al. (2010, 2013)
Angular diameter	0.079 ± 0.002 mas	Groote & Hunger (1982)
$\log T_{\text{eff}}$	4.352 ± 0.012	Groote & Hunger (1982) Reiners et al. (2000)
Spectroscopy		
$\log g$	4.2 ± 0.2	Shultz et al. (2019b)
$\log T_{\text{eff}}$	4.362 ± 0.04	Hunger et al. (1989)
$\log L/L_{\odot}$	3.50 ± 0.20	Shultz et al. (2019b)
$v \sin i$	140 ± 10 km s $^{-1}$	Oksala et al. (2012, 2015)
$\epsilon_{\text{C}} = \log \frac{N_{\text{C}}}{N_{\text{H}}}$	-4.5 ± 0.5 dex	Oksala et al. (2012, 2015)
$\epsilon_{\text{He}} = \log \frac{N_{\text{He}}}{N_{\text{H}}}$	-0.85 ± 0.25 dex	Oksala et al. (2012, 2015)

cluster. σ Ori E, in particular, at a *Gaia* DR2 angular distance of 80.4 arcsec on the sky from the cluster center has a parallax of 2.28 ± 0.10 mas, i.e. a distance of 439^{+20}_{-19} pc. This places it towards the furthest edge of the cluster (like for σ Ori C and D), as shown by the long-dashed vertical line in Fig. 2. This comes in contrast to the distance estimate of 387.5 ± 1.3 pc for the triple σ Ori A and B system determined by Schaefer et al. (2016) from interferometric measurements (no *Gaia* DR2 parallax is available for σ Ori AB as it is too bright). The various astrometric quality checks are nevertheless good for σ Ori E: ten visibility periods are used in the astrometric calculation, the astrometric excess noise of 0.25 mas is not significant, and the

Table 2. Properties of σ Ori E to be fitted by stellar models.

Radius.	$3.73 \pm 0.26 R_{\odot}$
Surface equatorial velocity	159 ± 11 km s $^{-1}$
P/P	1.34 ± 0.10 My
$\log L/L_{\odot}$	3.50 ± 0.19
$\log T_{\text{eff}}$	4.352 ± 0.012

parallax uncertainty is less than 5% (see below). The distance to σ Ori E derived from the *Gaia* DR2 parallaxes should thus be reliable.

The parallax uncertainties are shown in Fig. 3 versus parallaxes for all stars within a sky distance of 20 arcmin of the cluster center. The great majority of stars with parallaxes between 2 mas and 3 mas, i.e. potential cluster members, have a parallax uncertainty better than 20%, and almost half of them, including σ Ori E, have parallax uncertainties better than 5%.

An estimate of the systematic parallax uncertainties is more difficult to evaluate, as it depends on many factors (see Luri et al. 2018). If we take the systematic uncertainty of 0.029 mas derived by Luri et al. (2018) from the distribution of quasars, the corrected distance to σ Ori E would be 433 pc, which is within the uncertainties of the uncorrected distance.

With respect to the DR2, the early DR3 (EDR3) still allows a slight improvement of the parallax. It gives a parallax of 2.31 ± 0.06 mas implying a distance of 433 ± 11 pc. This EDR3 distance is good agreement with the distance of 439 pc obtained above from DR2.

In addition, new photometric attributes published in EDR3 from the Image Parameters Determination (IPD) module (Lindgren et al. 2020) confirm the absence of significant flux structures in the image window around σ Ori E. A first parameter, `ipd_frac_multi_peak`, indicates the fraction of valid transits for which another peak is observed in the image window around the source. For σ Ori E, this parameter equals zero, which means that only one peak is detected in the image window of σ Ori E for all transits used in the astrometric solution. A second parameter, `ipd_gof_harmonic_amplitude`, with a small value of 0.015 for σ Ori E, indicates that the goodness-of-fit of the flux distribution is independent of scan angle. Both these indicators point to the absence of significant structures of the flux distribution around σ Ori E such as could result from the presence of a second source or of specific patch patterns around the source, and thereby support the reliability of the distances derived from DR2 and EDR3 parallaxes.

2.2. Observed properties of σ Ori E

In Table 1, we have collected the data deduced from observations characterizing σ Ori E (HD 37479). The angular diameter, $\theta = 0.079 \pm 0.002$ mas, has been obtained by Groote & Hunger (1982) through the formula $\theta = 2(F_{\text{earth}}/F_{\text{theo}})^{1/2}$, where F_{earth} is the integrated flux received on Earth, and F_{theo} is a theoretical absolute flux determined using Kurucz' model atmospheres.

Using the distance determined by *Gaia* (DR2, 439^{+20}_{-19} pc) and the angular diameter, one can determine the radius of σ Ori E ($3.73 \pm 0.26 R_{\odot}$). The effective temperature (22500 ± 600 K) is deduced from the flux received on Earth and the angular diameter. This value is in agreement with the spectroscopic determination of the effective temperature by Hunger et al. (1989). Note that a recent determination by Oksala et al. (2012), using high resolution spectropolarimetry finds an effective temperature around

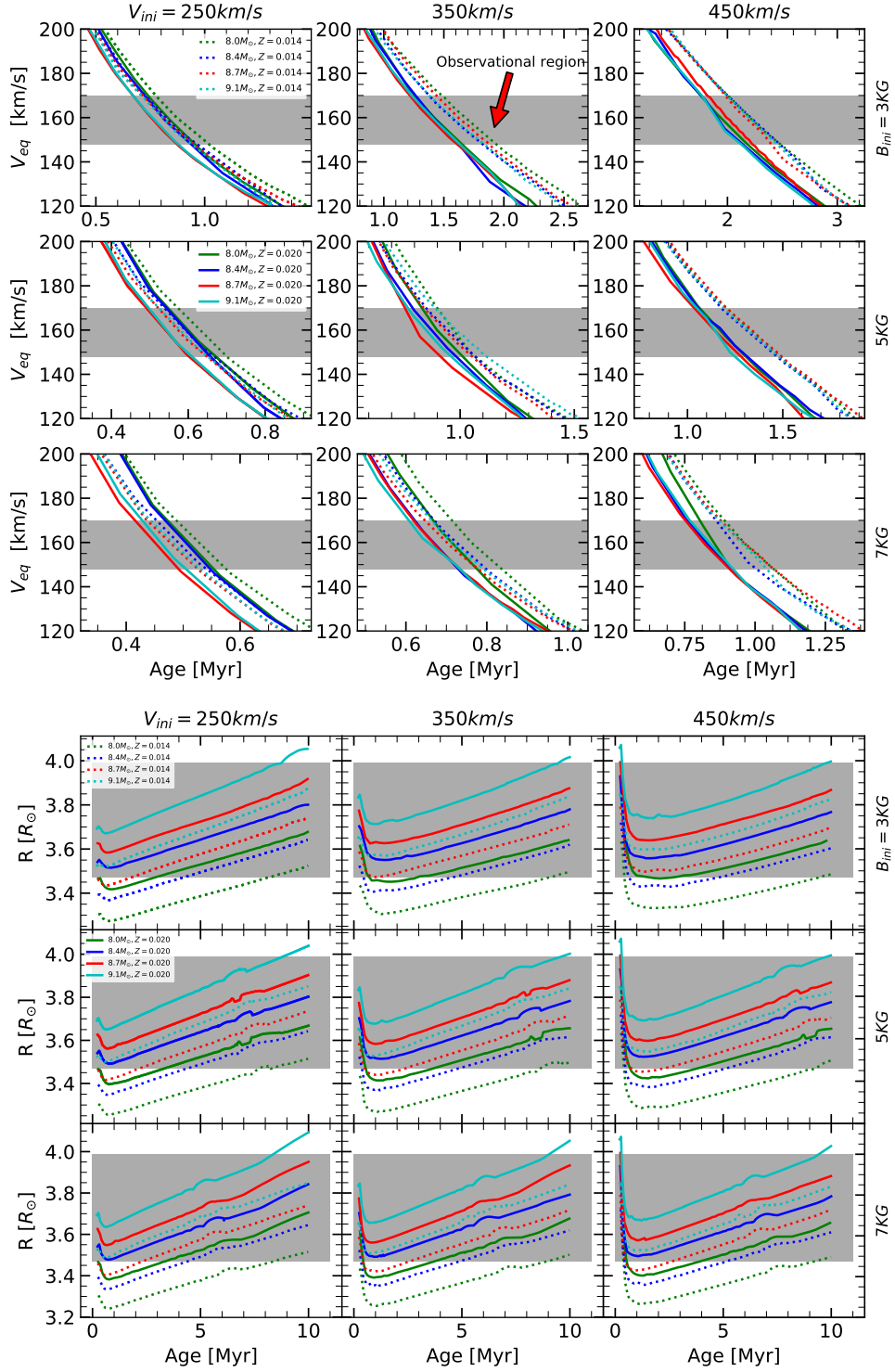


Fig. 4. *Top panel:* Evolution of the surface equatorial velocity as a function of the age of the star for stellar models with various initial masses, metallicities, rotations, and surface magnetic fields. The shaded areas show the range of values for the surface equatorial velocity that can be deduced from the observed rotational period and from the stellar radius determined from the angular diameter and the Gaia distance. *Bottom panel:* Evolution of the stellar radius as a function of the age of the star for stellar models with various initial masses, metallicities, rotations, and surface magnetic fields. The light shaded area show the range of values for the stellar radii that can be deduced from from the angular diameter and the Gaia distance.

23000 ± 3000 K², also not fundamentally different from the one obtained by Groote & Hunger (1982). From the rotational period and the radius of the star, one can deduce the surface equa-

² These authors however have not modeled in detail the spectrum and did not attempt to determine precisely the effective temperature.

torial velocity (159 ± 11 km s⁻¹). Using the radius and the effective temperature, one can determine the luminosity of σ Ori E quoted in Table 2. This luminosity is in agreement with the spectroscopically determined one by Shultz et al. (2019b), see Table 1. Shultz et al. (2019b) provides also a value for the effective gravity also shown in Table 1.

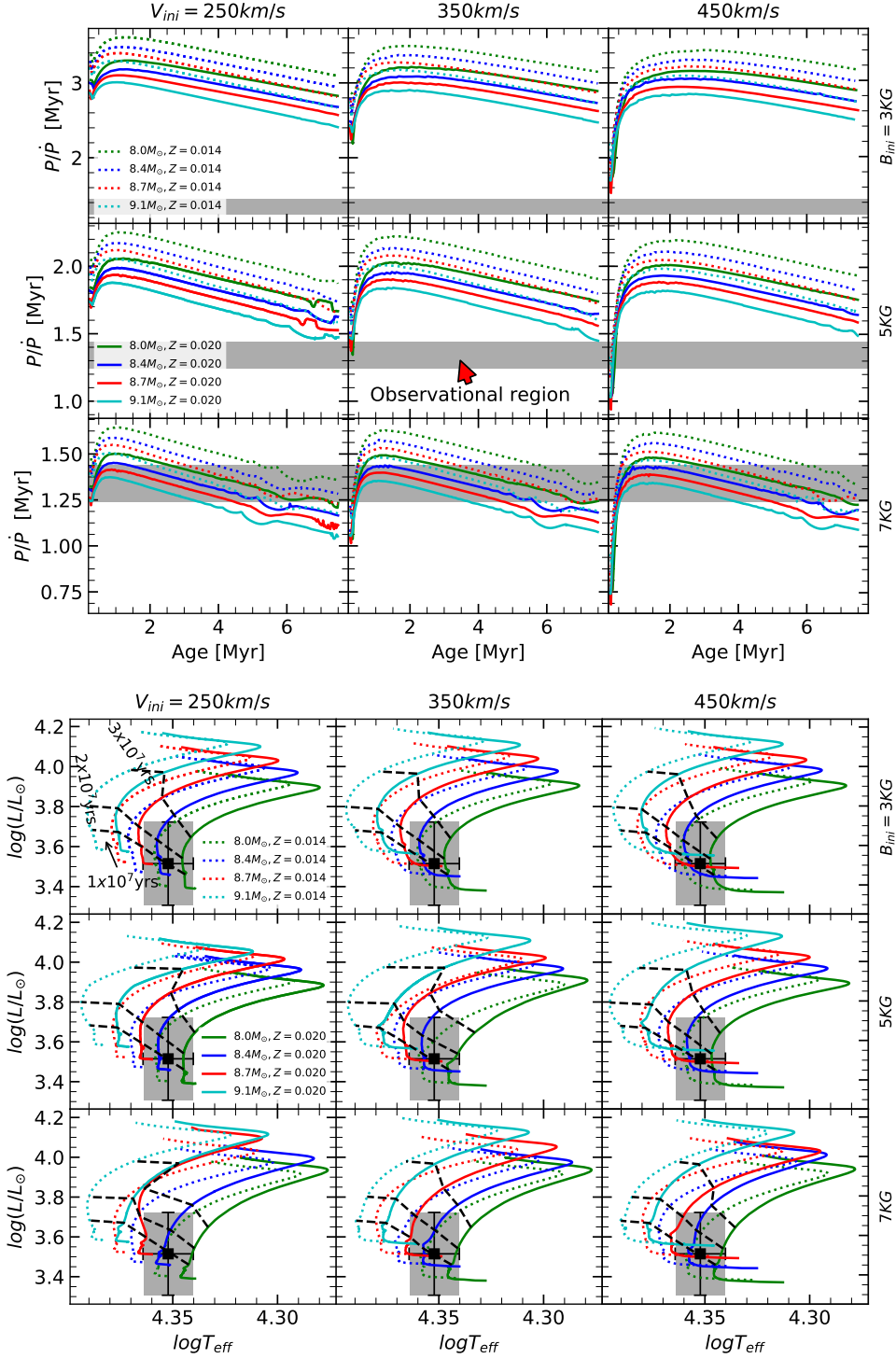


Fig. 5. *Top panel:* Evolution of \dot{P}/P , where P is the rotation period, for stellar models with various initial masses, metallicities, rotations, and surface magnetic fields. The light shaded area show the range of values for the braking timescale as deduced by Townsend et al. (2010). *Bottom panel:* Evolutionary tracks for stellar models with various initial masses, metallicities, rotations, and surface magnetic fields. Three black dashed lines indicate the isochrones with ages ranging from 10 Myr to 30 Myr. The position of σ Ori E is indicated.

We do not consider the surface magnetic field as well as the surface abundances as constraints of the present models. As indicated in the previous section, the actual morphology of the surface magnetic field is more complex than the one used here to model the wind magnetic braking. So the only quantity that we can hope to obtain is the value of an equivalent surface equatorial magnetic field in a pure aligned dipolar morphology that can

fit both the surface rotation and the spin-down timescale. The fitting value provides an estimate of the field but can differ from the observed one.

σ Ori E presents surface chemical inhomogeneities likely produced by microscopic diffusion that might occur in atmosphere stabilized by a strong magnetic field (see *e.g.* Michaud 1970). In the entire class of Bp/Ap stars, these chemical inho-

Table 3. For each stellar model characterized by an initial mass, metallicity, rotation and surface magnetic field is indicated the age range where the model fits the observed surface velocity, the observed radius and the observed braking timescale. The column labeled by HRD indicates whether the model fits (Y) or not (N) the observed position in the HR diagram. Red colors indicate age ranges and HRD positions that are not compatible with the the age range given by the surface velocity constraint. Only seven models highlighted with bold face satisfy all the constraints considered in this table.

M_{ini} M_{\odot}	v_{ini} $\frac{\text{km}}{\text{s}}$	$B_{\text{eq,ini}}$ kG	Age ranges in Myr deduced from				Age ranges in Myr deduced from			
			v_{eq}	R	$\frac{P}{P_{\odot}}$	HRD	v_{eq}	R	$\frac{P}{P_{\odot}}$	HRD
Z=0.014										
8.0	250	3	0.81-1.02	> 8.20	No Sol.	Y	0.74-0.95	>3.0	No Sol.	Y
8.4	250	3	0.72-0.96	> 4.25	No Sol.	N	0.73-0.94	>0.0	No Sol.	Y
8.7	250	3	0.72-0.94	>1.70	No Sol.	N	0.67-0.87	>0.0	No Sol.	Y
9.1	250	3	0.71-0.94	> 0.0	No Sol.	N	0.67-0.88	0.00-8.7	No Sol.	N
8.0	250	5	0.56-0.70	> 7.8	No Sol.	Y	0.55-0.67	>3.3	No Sol.	Y
8.4	250	5	0.53-0.67	>4.5	No Sol.	N	0.54-0.66	>0.0	No Sol.	Y
8.7	250	5	0.52-0.65	>2.0	No Sol.	N	0.48-0.60	>0.0	No Sol.	Y
9.1	250	5	0.52-0.65	>0.0	No Sol.	N	0.50-0.61	0.00-8.80	No Sol.	N
8.0	250	7	0.49-0.57	>8.4	>5.2.	Y	0.47-0.55	>3.5	<0.5 or 2.6-7.3	Y
8.4	250	7	0.45-0.54	>4.5	<0.3 or >3.9	N	0.47-0.55	>0.0	<0.7 or 1.4-5.3	Y
8.7	250	7	0.43-0.53	>2.3	<0.4 or >3.	N	0.42-0.49	>0.0	<4.5	Y
9.1	250	7	0.44-0.53	>0.0	<0.4 or >2.1	N	0.43-0.51	<8.40	<3.4.	N
8.0	350	3	1.48-1.92	>9.3	No Sol.	Y	1.25-1.65	<0.7or >2.8	No Sol.	Y
8.4	350	3	1.38-1.81	>4.6	No Sol.	Y	1.25-1.63	>0.0	No Sol.	Y
8.7	350	3	1.44-1.86	>0.0	No Sol.	Y	1.20-1.60	>0.0	No Sol.	Y
9.1	350	3	1.38-1.81	>0.0	No Sol.	N	1.23-1.63	<9.5	No Sol.	Y
8.0	350	5	0.90-1.06	>8.7	No Sol.	Y	0.83-1.02	>4.7	<0.3 or > 7.5	Y
8.4	350	5	0.85-1.06	>4.8	No Sol.	Y	0.79-0.98	>0.0	<0.3 or > 7.5	Y
8.7	350	5	0.84-1.04	>2.5	No Sol.	N	0.75-0.91.	>0.0	<0.3 or > 7.5	Y
9.1	350	5	0.89-1.04	>0.0	No Sol.	N	0.77-0.96.	<9.5	No Sol.	Y
8.0	350	7	0.72-0.83	>9.1	<0.5 or >5.9	Y	0.67-0.77	<0.5 or >3.9	0.3-0.7 or > 2.8	Y
8.4	350	7	0.67-0.80	>4.9	0.3-0.5 or >4.3	Y	0.62-0.73	>0.0	0.3-5.7.	Y
8.7	350	7	0.65-0.77	>2.5	0.3-0.5 or >3.3	N	0.62-0.73	>0.0	0.4-4.7	Y
9.1	350	7	0.67-0.78	>0.0	0.3-0.6 or >2.3	N	0.61-0.73	0.0-9.0	0.5-3.7	Y
8.0	450	3	2.00-2.50	0.00-0.50 or >9.5	No Sol.	Y	1.76-2.17	>0.0	No Sol.	Y
8.4	450	3	2.00-2.50	0.00-0.60 or >4.8	No Sol.	Y	1.76-2.15	>0.0	No Sol.	Y
8.7	450	3	1.98-2.40	> 0.0	No Sol.	Y	1.81-2.13	>0.25	No Sol.	Y
9.1	450	3	1.99-2.45	> 0.0	No Sol.	N	1.76-2.23	0.35 - 9.6	No Sol.	Y
8.0	450	5	1.19-1.49	0.00-0.40 or >9.2	0.3-0.4	Y	1.06-1.36	<0.7 or >3.9.	0.35-0.50	Y
8.4	450	5	1.17-1.47	0.00-0.50 or >5.2	0.3-0.4	Y	1.06-1.37	>0.0	0.35-0.50	Y
8.7	450	5	1.19-1.49	0.00-0.70 or >2.3	0.3-0.4	Y	1.03-1.32	>0.2	0.35-0.50	Y
9.1	450	5	1.18-1.47	>0.0	0.0-0.4	N	1.04-1.31	>0.3.	0.30-0.40.	Y
8.0	450	7	0.88-1.07	0.00-0.40 or >9.3	0.4-0.6 or >6.0	Y	0.80-0.91	<0.5 or >4.1	0.4-0.8 or 2.8-7.2	Y
8.4	450	7	0.86-1.00	0.00-0.40 or >5.2	0.4-0.6 or >4.6	Y	0.76-0.91	>0.0	0.4-6.0	Y
8.7	450	7	0.87-1.07	0.00-0.50 or >2.7	0.4-0.6 or >3.4	N	0.75-0.91	>0.2	0.5-5.0	Y
9.1	450	7	0.87-1.03	>0.0	0.4-0.8 or >2.4	N	0.77-0.92	0.3-9.5	0.5-3.8	Y

mogeneities have been well documented for decades (Babcock 1947; Wolff 1968; Landstreet & Borra 1978). Recently Panei et al. (2021) have explored the questions of chemical inhomogeneities at the surface of magnetic early B-stars. Since these processes are not accounted for in the present models, we cannot use the observed surface abundances as constraints. On the other hand, we may see whether rotational mixing is expected to have occurred in σ Ori E. As we shall see, the age we obtain is too short for rotational mixing as included in the present models to have a sensible effect.

3. Physics of the models

Stellar models are computed with GENEC, the Geneva stellar evolution code. The physical ingredients are the same as those of Ekström et al. (2012a) for what concerns any non-magnetic effects. We use the Schwarzschild criterion for convection with a modest overshooting given by an extension of the radius of $0.1 H_p$, where H_p is the pressure scale height estimated at the

Schwarzschild boundary. Rotational mixing is accounted for according to the shellular theory by Zahn (1992). The diffusion coefficients and the physics of rotation are implemented as explained in Ekström et al. (2012a). The mass-loss rate via stellar winds is used according to de Jager et al. (1988). The present rotating models account for the various effects of a surface magnetic field on massive star evolution (Meynet et al. 2011; Petit et al. 2017; Georgy et al. 2017; Keszthelyi et al. 2019, 2020).

Similarly to previous GENEC implementations (Meynet et al. 2011; Georgy et al. 2017; Keszthelyi et al. 2019), we account for wind magnetic braking and mass-loss quenching. The wind magnetic braking is accounted for following the recipe given by ud-Doula et al. (2009). The present magnetic braking timescale of 1.3 Myr was found well in the range of values expected from the theory of wind magnetic braking given in ud-Doula et al. (2009) supporting thus the view that the observed braking might be due to that process.

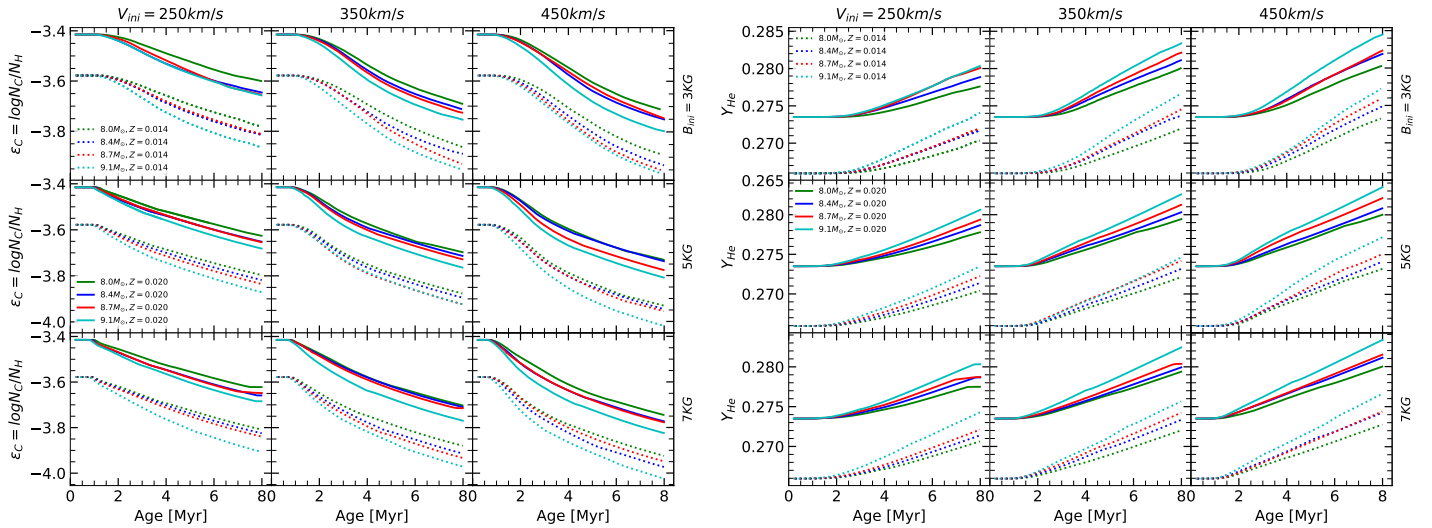


Fig. 6. Evolution of the abundance ratios in number at the surface as a function of time. *Left panel:* the ratio of carbon to hydrogen. *Right panel:* the ratio of helium to hydrogen.

The rate of loss of spin angular momentum \dot{J}_{mb} due to magnetic braking is expressed by

$$\dot{J}_{mb} = \frac{2}{3} \dot{M}_{wind} \Omega R^2 [0.29 + (\eta_* + 0.25)^{1/4}]^2, \quad (1)$$

where \dot{M}_{wind} is the mass-loss rate the star would have in absence of the magnetic field (this is $\dot{M}_{B=0}$), Ω the surface angular velocity, R , the stellar radius, $\eta_* = \frac{B_{eq}^2 R^2}{M v_\infty}$ the equatorial magnetic confinement parameter (ud-Doula & Owocki 2002) with B_{eq} the equatorial magnetic field which is equal to half the polar field in case of a dipolar magnetic field aligned with the rotational axis, v_∞ is the final wind velocity (*i.e.* the wind velocity when there is no longer acceleration). The quantity $R[0.29 + (\eta_* + 0.25)^{1/4}]$ is the Alfvén radius, R_A .

Since magnetic braking modifies the angular velocity of the stellar surface, the Geneva code implements equation (1) as a boundary condition of the internal angular momentum transport equation at the stellar surface, and modifies the total angular momentum content of the star.

We have implemented the effect of mass-loss quenching by the surface magnetic field in the same way as Petit et al. (2017). We assumed that the magnetic field is constant in time (see the discussion in Sect. 5). The escaping wind fraction f_B (number inferior to 1) is taken as

$$f_B = \frac{\dot{M}_{wind}}{\dot{M}_{B=0}} = 1 - \sqrt{1 - \frac{R}{r_c}}, \quad (2)$$

where r_c is the radius of the farthest closed loop of the magnetic field and is computed as a function of the Alfvén radius and the confinement parameter (for details, see (Keszthelyi & Petit 2017; Petit et al. 2017; ud-Doula & Owocki 2002)). We did not account for the factor $1 - \sqrt{1 - 0.5R/R_K}$, where R_K is the Kepler corotation radius defined by $R/W^{2/3}$, with $W = V/\sqrt{GM/R}$ (see Eq. 22 in Ud-Doula et al. 2009). The quantity W is the ratio of the surface rotation to the Keplerian critical velocity *i.e.* the velocity at which, keeping the stellar radius constant, the centrifugal acceleration balances the gravity at the equator. Not accounting for this factor (as done here) overestimates the effect of the magnetic mass loss quenching. We note however that this does not impact the angular momentum loss rate since this one

depends on the mass loss rate in absence of any magnetic mass loss quenching. The reason for this is that the mass retained in the magnetosphere slows down the star anyway and its effect is accounted for in the formula for the angular momentum loss. Thus we suspect that actually the mass loss quenching has here a rather modest effect by modifying the way the total mass of the star decreases. For the cases considered here the total mass removed remains anyway very modest. As a numerical example, a $9 M_\odot$ star has a mass loss rate between 10^{-9} and $10^{-10} M_\odot$ per year during the MS phase. Thus it loses a fraction of its total mass that is less than 0.3% during the 30 Myr duration of the MS phase. The magnetic mass loss quenching will still reduce that quantity. Typically considering for our $9 M_\odot$ star, a surface magnetic field of 5 kG, an average surface rotation during the MS phase of 200 km s^{-1} , we have that the Alven Radius R_A (about 30 times the stellar radius) is larger than the Keplerian Radius R_K (around 15 times the stellar radius). and we have thus here a centrifugal magnetosphere (Petit et al. 2013). In this case, rotation impacts significantly the dynamics of the magnetosphere (Townsend et al. 2005) and may lead to rotationally modulated variations of spectroscopic or photometric diagnostics (as e.g. Balmer lines, UV, X-rays, see eg. Petit et al. 2013). When the magnetic mass loss quenching is accounted for such a star, the mass lost during the MS phase is only a few percents of the mass lost without that effect and amounts to 0.01% of the total mass of the star. Note the considering the data for σ Ori E indicated in Table 1, assuming a mass around $9 M_\odot$, one obtains that the Alfvén radius is around 50 stellar radii and the Kepler radius is around 30 stellar radii.

For single star models, we considered models of 8.0, 8.4, 8.7 and $9.1 M_\odot$ with metallicities, $Z=0.014$ and 0.020 , with initial rotations equal to 250, 350 and 450 km s^{-1} , and an equatorial surface magnetic field of 3, 5 and 7 kG.

4. Models for σ Ori E

Figures 4 and 5 present the evolution as a function of time of the surface equatorial velocity, of the stellar radius, of the braking timescale, as well as the evolutionary tracks in the HR diagram. The grey regions, in each panel, indicate the observed values of the different physical quantities. In Table 3, each model

is specified by its initial mass, rotation, surface magnetic field (see columns 1 to 3), the age range where the model can fit the surface velocity, the stellar radius and the braking timescale (see columns 3 to 4 for the models with a metallicity equal to 0.014, and columns 7, 8 and 9 for the metallicity equal to 0.020). Columns 6 and 10 indicate whether the position of the star in the HR diagram can be fitted (Y) or not (N). When for the age ranges, No Sol. is indicated, it means more precisely that there is no solution in the age range between 0 and 10 Myr. We have used red colors to emphasize age ranges that are not coincident with the one given by the requirement of fitting the surface velocity. Boldfaced age ranges highlight the domains of ages allowing a simultaneous fit of all the constraints indicated in Table 2.

4.1. Theoretical predictions

As shown in the left panel of Fig. 4, the surface equatorial velocity decreases as a function of time. A consequence of the strong surface rotation decrease is that very rapidly the star has a surface velocity that corresponds to a modest ratio of the critical velocity. The critical velocity is the surface equatorial velocity the star should have in order for the gravity at the equator to be balanced by the centrifugal force. As a numerical example, the critical surface velocity of stars³ with an initial mass between 8 and 9.1 M_{\odot} and a radius compatible with the one indicated in Table 2 for σ Ori E is between 506 and 578 km s^{-1} . Models that satisfy the observed constraints have surface velocities between 150-170 km s^{-1} . This represents a surface velocity equal to 26-34% of the critical values. This is a too low ratio for rotation to have any significant effect on the shape of the outer layers.

From the left panel of Fig. 4, we see that for a given initial rotation, the results do not show a great sensitivity on the changes of the initial mass in the narrow mass interval between 8.0 and 9.1 M_{\odot} . Increasing the surface magnetic field implies, as expected, a stronger braking. A given surface velocity is thus reached at an earlier time. The models at $Z=0.014$ shows a higher surface rotation at a given age than those at $Z=0.020$. When the metallicity decreases, stars are more compact and have weaker stellar winds, this decreases, at a given surface rotation rate, the loss of angular momentum and thus increases the braking timescale. Let us recall that a scaling of the wind with metallicity of the form $\dot{M}_{\text{wind}} \propto (\frac{Z}{Z_{\odot}})^{0.5}$ has been used here (as in the Geneva grids of stellar models Ekström et al. 2012a; Georgy et al. 2013).

The evolution of the stellar radii is shown in the upper panel of Fig. 4. Each curve shows two parts: a first short phase where the radius decreases and a second long phase during which it increases. The first phase is due to the very efficient slowing down of the star by the magnetic wind braking effect. To understand this, it is important to remind that rotation deforms the star making it oblate. Thus the radius plotted in this panel is actually an average radius, defined as the radius of a spherical star that would have the same volume as the rotationally deformed star. Since the polar radius is not significantly changed by rotation (see Fig. 2 in Ekström et al. 2008), and since the equatorial radius increases when rotation increases, the volume of a star increases with rotation (Keszthelyi et al. 2020). When the star is braked down, its volume decreases. This explains the first short decreasing phase. At a given time, the braking timescale becomes long enough for the secular evolution of the star to become the main agent driving the evolution of the radius. As is well known, dur-

ing the MS phase the radius increases and this is what we see in that second phase. The first phase last longer for the models starting with a high initial rotation. It becomes shorter for the models with a high surface magnetic field. As is well known, models at $Z=0.014$ have smaller radii at a given age than models at $Z=0.020$ (the difference of stellar radius is approximately 0.2 R_{\odot} between the two models with different metallicities).

The evolution of the braking timescale is shown in the left panel of Fig. 5. We can identify the two phases coming from the evolution of the radius just described above. In the first phase, the braking timescale increases rapidly due to the rapid slowing down of the star. It reaches a maximum then decreases. The decrease is mainly due to the fact that the mass loss rate and the stellar radius increase during the evolution along the MS phase. Models with $Z=0.014$ show longer braking timescales than those with $Z=0.020$. At lower metallicity the stars are more compact and the stellar winds are weaker thus the angular momentum loss rate, at a given surface velocity, are weaker. We see that, for each model, a given braking timescale, in a fixed range different for each model, may occur at two different ages of the star. One at the very early time and one at a time when the age of the star is significantly above the braking timescale. This is due to the evolution described above.

In the lower panel of Fig. 5, we also see that lowering the metallicity shift the tracks to hotter parts of the HR diagram. We see the consequences on the HR diagram of the short first phase during which, due to braking the average radius decreases. This corresponds to the phase, at the very beginning of each track, that is nearly horizontal. The luminosity keeping constant, the effective temperature increases. Note that the effective temperature defined here is also an average effective temperature. Indeed, due to the von Zeipel theorem (von Zeipel 1924), the effective temperature varies as a function of the latitude when the star is rotating, the poles being hotter than the equatorial regions. The effective temperature plotted in the figure is obtained as $L/(4\pi R^2)$, where R is the average radius.

4.2. Comparisons with σ Ori E

Using Figs 4 and 5 (only the top panel), we can derive the range of ages of the models when they are inside the grey zone, *i.e.* fit the corresponding property of σ Ori E deduced from the observations. The bottom panel of Fig. 5 does not directly allow to deduce the age range (although some constant age lines are shown) but allows us to see whether the beginning of the tracks goes through the observed position of σ Ori E in the HR diagram.

The constraint coming from the surface velocity points towards a young star (see columns 4 and 8 of Table 3) with an age between 0.4 and 2.5 Myr for all masses, initial rotations, metallicities or surface magnetic fields considered here. Among the other three constraints, the one on the magnetic braking timescale (see columns 6 and 10) is the most efficient in eliminating many models.

For the metallicity $Z=0.014$, actually no models is found having a P/\dot{P} compatible with the one observed in the age range given by the observed surface equatorial velocity (although sometimes the miss is due to a rather small incompatibility). The constrain of the radius at $Z=0.014$ points to older ages than those needed to account for the surface velocity except in the case of the 8.7-9.1 M_{\odot} stellar models that are compatible with very young ages. The position in the HR diagram at $Z=0.014$ favors masses around 8.0-8.7 M_{\odot} .

³ We assume here a Roche model where the critical velocity is given by $\sqrt{\frac{2GM}{3R}}$.

For the metallicity $Z=0.020$, only models with a surface equatorial magnetic field around 7 kG provide a simultaneous fit to the constraints indicated in Table 2. Depending on the initial rotation, the age is either between 0.4-0.5 (250 km s^{-1}), 0.6-0.7 (350 km s^{-1}) or 0.75-0.9 (450 km s^{-1}). As already mentioned above, for a given surface magnetic field, starting from a larger rotation allows the star to reach the observed surface velocity at a later time. At $Z=0.020$, except for some models starting with 250 km s^{-1} , the position in the HRD can always be fitted.

The finding of consistent solutions is thus easier at $Z=0.020$ than at $Z=0.014$. In Table 3, we have highlighted in boldface the range of ages where all the five constraints shown in Table 2 can be fitted. As mentioned above, only models at $Z=0.020$ are found. Actually we cannot say that models with a metallicity $Z=0.014$ reproducing the observed properties of σ Ori E do not exist, because we did not explore changes in the mass loss rates, convective core size, different angular momentum transport for instance. But it would bring us too far to explore all these possibilities, especially because, as discussed below, a metallicity of $Z=0.020$ for σ Ori E is not unreasonable at the moment.

Taken at face, the above results show that the models that best match the observed properties of σ Ori E have the following properties: the initial mass is between 8.4 and $9.1 M_{\odot}$, the metallicity is around $Z=0.020$, the age is between 0.4 and 0.9 Myr, and finally the magnetic braking is similar to the one due to a dipolar aligned magnetic field with an equatorial value of ~ 7 kG. The high surface rotation and magnetic field of σ Ori E is possible because it is a very young single star.

We could have used as an additional constraint the surface gravity that is 4.2 ± 0.2 (see Table 1) according to Shultz et al. (2019b), but it would not help constraining more the model. Indeed for all the four initial masses considered here, between 8.0 and $9.1 M_{\odot}$, the minimum and maximum radii allowed by the measured surface gravity define a region that overlaps and extends beyond the shaded region shown in the bottom panel of Fig. 4. Thus any solution fitting the radius will fit the constraint of the surface gravity.

Figure 6 shows the evolution of the surface abundances of carbon and helium as a function of time. We see that the changes in helium abundances is very small with respect to those of carbon (the abundance of carbon is normalized to that of hydrogen, while the abundance of helium is not. However hydrogen does not change much and most of the variation shown for carbon is due to the change of carbon only). For carbon, models predict a decrease by a factor 2 (0.3 dex) already after 8 Myr and for the models with an initial rotation larger than $\sim 350 \text{ km s}^{-1}$. Helium needs much more time than carbon to show changes at the surface. This effect is due to the following facts: first let us recall that the diffusive velocity for a given element i scales as $\frac{1}{X_i} \frac{\Delta X_i}{\Delta r}$, where X_i is the mass fraction of the element and $\Delta X_i / \Delta r$ is the gradient of the abundance of this element. At the beginning there is no gradient, Zero Age Main-Sequence models being chemically homogeneous. In absence of any mixing in the radiative zones, the gradients between the core and the envelope then evolve under the actions of both nuclear burning and convection. Helium increases at the center and carbon decreases due to the action of the CN cycle. The CN cycle is very rapid, much more rapid than the synthesis of helium. After one million year, in a $9 M_{\odot}$, the difference between the mass fraction of helium in the core and that in the envelope is 0.11 (in the core one has a mass fraction of 0.277 and in the envelope of 0.266). For the carbon we have in the core a mass fraction of 0.00003 and in the envelope the value is 0.0023. A rough estimate of the ratio of

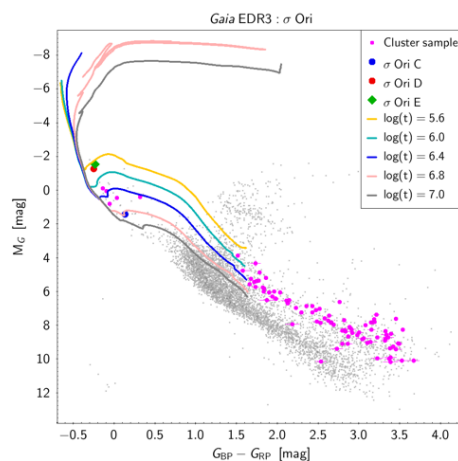


Fig. 7. Observed positions in the *Gaia* observational HR diagram of potential (see text) members of the σ Orionis cluster (black filled circles), with *Gaia* sources in the cluster field of view with parallaxes better 10% shown in small gray points in the background. The uncertainties due to both photometry and parallax uncertainties are shown for all cluster members, being for the majority of them smaller than the size of the points. Superposed are shown isochrones for a metallicity $Z=0.014$ from Haemmerlé et al. (2019) for different values of the logarithm of the age (in years). The positions of σ Ori C, D and E are highlighted in the diagram as shown in the inset.

the diffusive velocity over the same value of Δr will therefore be $V_{\text{He}}/V_{\text{C}} \approx 0.011/0.271 \times 0.0012/0.0023 \sim 0.02$. Thus the diffusive velocity of helium is about only 2% the diffusive velocity of carbon, hence the surface will show signs of the CN cycle before any significant change of helium.

The value quoted by Oksala et al. (2012, 2015) (see Table 1 and Sect. 5.2) for the abundance of carbon (between -4.0 and -5.0 dex, see table 1) cannot be reached at any time by the present models (actually the most massive models at $Z=0.014$ can just reach value just below -4 dex after 8 Myr). It would be very interesting to have data for the nitrogen abundances to see whether this low carbon might be associated with an increase in nitrogen abundances. This would indicate the presence at the surface of material having been processed by the CN cycle, that very rapidly reaches equilibrium at the centre.

The observed helium surface abundance available at the moment, (ϵ_{He} between -1.1 dex and -0.6 dex) span a very large domain. σ Ori E presents a non homogeneous surface composition due to processes as microscopic diffusion in regions of the star where a strong magnetic field allow to stabilize the atmosphere. Atomic diffusion like in Ap/Bp stars would mostly impact heavier elements, like Si and Fe-group, producing an anomaly with an overabundance in some and an under-abundance in others. We have not accounted for such processes in our models thus we can not make comparisons with the observed surface abundances. On the other hand, Fig. 6 shows that, for the very small ages obtained for σ Ori E using the present models (below 1 Myr), no changes of the surface composition due to rotational mixing (as accounted for in the present models) is expected.

5. Discussion

5.1. The age of σ Ori E and the age of the σ Orionis open cluster

Since the star σ Ori E belongs to the σ Ori cluster, we can wonder whether estimating the age of the cluster through isochrone

fitting gives values that are compatible with the age deduced above for σ Ori E based on fitting the surface rotation, the radius, the braking timescale and the position in the HR diagram. Let us remind that Sherry et al. (2008); Caballero (2007) have obtained using this technics ages between 2-3 Myr, thus larger than the ages inferred for σ Ori E in the present work. However, as is well known, age determination is a very model dependent process.

We present in Fig. 7, the positions in the observational HR diagram of a sample of member candidates to the σ Ori cluster using *Gaia* EDR3 photometry and parallax. The member candidates are selected from an initial sample of sources within a circle of 600 arcsec radius around the center of the cluster center, with the conditions $2 < \varpi$ [mas] < 3 on the parallax, $0.2 < \text{PM}_{\text{RA}}$ [mas/yr] < 2.5 on the right-ascension proper motion and $-2.2 < \text{PM}_{\text{DEC}}$ [mas/yr] < 0.5 on the declination proper motion. These selection criteria favor purity of cluster membership rather than completeness. The candidates have further been restricted to those brighter than 19 mag in *G* and having uncertainties in $G_{\text{BP}} - G_{\text{RP}}$ less than 0.1 mag. The $G_{\text{BP}} - G_{\text{RP}}$ uncertainties and the ones of the absolute *G* magnitude are shown in Fig 7. with horizontal and vertical bars, respectively, the latter uncertainty including both photometric and parallax uncertainties. These uncertainties are smaller than the size of their data points in the figure for the great majority of the member candidates. It must be noted that past studies of this cluster conclude on very little reddening of its members (Béjar et al. 2001; Oliveira et al. 2002). We therefore did not apply any reddening correction.

Superposed are shown isochrones for different ages between 0.4 Myr ($\log(t) = 5.6$) and 10 Myr ($\log(t) = 7.0$) accounting for the pre-Main-Sequence phase computed with accretion and no rotation by Haemmerlé et al. (2019) and a metallicity $Z=0.014^4$. The isochrone passing through the observed position of σ Ori E is either an isochrone corresponding to a very young age with a log age between 5.6 and 6.0 or an isochrone with a log age larger than 7 (not shown here). However, a young age is likely the most reasonable solution in case most of the stars below a magnitude *G* equal to 4.0 are indeed pre-MS stars. Thus it appears that an age of 1 Myr for σ Ori E as deduced above, based on fitting the observed properties of σ Ori E, does not appear in contradiction with the age determined by isochrone fitting. We note however that this aspect would need a more careful analysis and also a trial with similar isochrones but computed with a metallicity $Z=0.020$.

5.2. The metallicity of σ Ori E

A solution is obtained only if the metallicity is around $Z=0.020$. A value of 0.014 makes the finding of a solution more difficult if not impossible. Since σ Ori E presents surface chemical inhomogeneities, direct determinations of its metallicity may be problematic. Oksala et al. (2015) in their Table 1 indicate values for $\epsilon_{\text{Fe}} (= \log(N_{\text{Fe}}/N_{\text{H}}))$ between -5.7 and -4.0 for σ Ori E. For comparison, the solar values in the same units as in Oksala et al. (2015) given by Scott et al. (2015) is -4.53. The large domain given by Oksala et al. (2015) does not allow to conclude whether σ Ori E is metal deficient or, on the contrary, slightly metal-rich compared to the Sun. Also, as already mentioned above, the Oksala's abundances may not reflect the bulk iron abundance in the

star and result of some diffusion processes unevenly affecting its surface composition. To obtain an idea of the actual metallicity, it is better to rely on measurements of normal stars belonging to the same association. According to Cunha et al. (1998), the star HD 294297 belongs to the Ori OB 1b Association where the σ Orionis cluster lies. They obtain an iron abundance (ϵ_{Fe}) of -4.68 ± 0.14 , thus below the solar abundance. If we assume that $Z/Z_{\odot} = 10^{\epsilon_{\text{Fe}} - \epsilon_{\text{Fe}\odot}}$ (i.e. assuming a solar scaled distribution of the heavy elements), then it would mean that Z would be equal to $0.71Z_{\odot}$, thus 0.010 with $Z_{\odot}=0.014$. Taken at face, if this metallicity is also the one corresponding to σ Ori E then our $Z=0.020$ model would not be an acceptable solution. In that case, either other parameters of the models should be changed to check whether a solution can be found at a metallicity lower than 0.020, or a more complex scenario involving multiple stars, like, for instance, a merging of two stars has to be invoked. However at the moment it is difficult to discard the $Z=0.020$ single star evolution scenario on the basis of this metallicity measurement. If we look at Table 2 of Cunha et al. (1998), and compare the iron abundances for stars belonging to one association (here Ori OB 1c), it goes from -4.8 ($0.54 Z_{\odot}=0.008$ applying the same rule as above) up to -4.41 ($1.32 Z_{\odot}=0.018$), which shows variations by a factor of 2.5! Moreover, Cunha et al. (1998) finds that the abundances of oxygen shows still greater diversity of abundances than iron. They suggest that some regions where the observed stars have formed have been enriched by a nearby supernova. This would have an impact on the mass fraction of heavy elements Z . Thus at the moment it is still difficult to reach a very strong conclusion until more data will be collected on the Ori OB 1b Association.

In this work we have not considered different initial helium mass fractions at a given metallicity. Decreasing helium at a given metallicity shifts the position of the evolutionary tracks in the HR diagram to the red may be allowing to find a solution for a metallicity equal to $Z=0.014$.

5.3. The magnitude of the surface magnetic field

The observed polar surface magnetic field of σ Ori E has been obtained by Oksala et al. (2012, 2015). According to Oksala et al. (2015), there is a dipolar component that is misaligned with respect to the rotation axis. The polar strength of this magnetic field is between 7.3 and 7.8 kG, with an obliquity between 47° - 59° but there is also a smaller non-axisymmetric quadrupole component with strength between 3-5 kG. Ideally of course one would need to produce a detailed modeling of the braking law resulting from the actual magnetic field topology. At the moment, based on the present simulations, we can only say that using an aligned dipolar configuration, we need a magnetic field polar strength that is around 14 kG, so larger than the observed one. Would a more realistic topology need a smaller polar field more in line with the observed one? Likely not, since both the misalignment and quadrupole components would be expected to decrease the braking efficiency overall compared to a pure aligned dipole. So this question at the moment remains open. Note that in this work we have not explored the possibility that the magnetic field flux may decay with time (discussions of possible underestimates of the braking efficiency and of the effect of magnetic flux decrease is discussed by Keszthelyi et al. 2021, in their study of the B-type star tau Sco). However the constraints given by the surface velocity and the isochrone fitting favors anyway a young age and thus a rather limited impact of this effect.

⁴ At the moment no such isochrones are available for a metallicity $Z=0.020$. A value of $Z=0.020$ would shift the isochrones slightly to the right in Fig. 7.

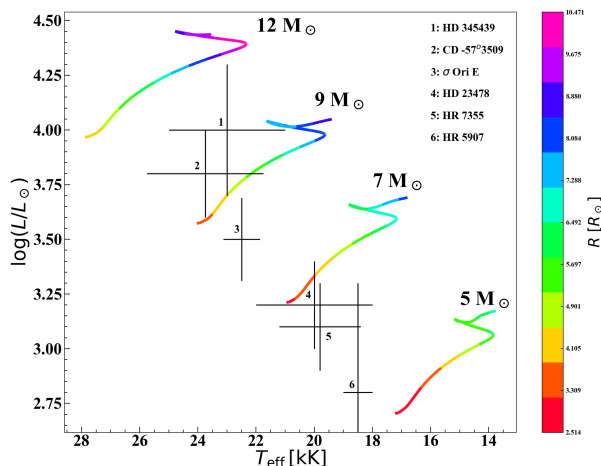


Fig. 8. Positions of σ Ori E and analogous stars in the HR diagram. The data for σ Ori E are those indicated in Table 2. For the other stars, the data have been taken as given in Table 1 of Shultz et al. (2020), except for the star CD -57°3509 taken from Przybilla et al. (2016). Main-Sequence rotating tracks from Ekström et al. (2012a) for the 5, 7, 9 and 12 M_{\odot} are indicated.

5.4. The timescale for diffusion

The star σ Ori E shows sign of the action of microscopic diffusion. One can wonder whether the small age obtained gives enough time for such a process to impact the surface composition. According to Fig. 8.1 of Michaud et al. (2015), the diffusion timescales in a stable atmosphere of a 2.5 M_{\odot} star are between 10^3 and 10^4 years depending on the element considered (the diffusion timescale is the time for a given chemical element to diffuse over a pressure scale height). These timescales are much shorter than the age derived here for σ Ori E. However, these estimates are based on a non-magnetic atmosphere and are valid for stars with an effective temperature less than 16 000 K. Above these temperatures, stellar winds are expected to prevent any stratification due to diffusion. In case of σ Ori E, the surface chemical inhomogeneities may be associated with regions stabilized by the strong magnetic field. Interestingly, the presence of a magnetic field does not change much the timescales indicated above (Georges Alecian, private communication and see also Fig. 1 in Stift & Alecian 2016). Thus, from this discussion, we conclude that diffusion has likely enough time to operate, at least in some stabilized regions, in timescales less than 1 Myr.

6. The σ Ori E analogs

In this section, we briefly discuss a few cases of σ Ori E analogs, *i.e.* of B-type stars presenting both a high surface rotation and a strong surface magnetic field. The positions of these stars in the HR diagram are shown in Fig. 8. In Table 4, some properties of such stars are listed together with those of σ Ori E. From the mean positions of these stars in Fig. 8 (not accounting for the error bars), we can deduce the mass and radius of each star as would be given by the stellar models and hence their critical velocity. Then from the $v \sin i$ indicated we obtain the minimum ratios of the actual equatorial to the critical velocity. We obtain

Table 4. Characteristics of some σ Ori E analogs ordered by decreasing $v \sin i$.

Name	type	$v \sin i$ [km s ⁻¹]	B_p [kG]	References
HR 7355	B2Vnp	300±15	11-12	[1]
HR 5907	He strong CP	290±10	10-16	[2]
HD 345439	He-rich B2V	270±20	-	[3]
σ Ori E	B2Vpe	160	7.3 - 7.8	[4]
HD 23478	He-norm B3IV	125±20	≥ 9.5	[5] [6]
CPD -57°3509	B2IV	70-250	3.3	[7]

[1] Rivinius et al. (2008, 2013); [2] Grunhut et al. (2012)
 [3] Eikenberry et al. (2014); [4] Oksala et al. (2015)
 [5] Eikenberry et al. (2014) [6] Sikora et al. (2015); [7] Przybilla et al. (2016)

values between about 25% (HD 23478) and 70% (HR 5907). According to Ekström et al. (2008), a 70% ratio makes the equatorial radius to be about 20% larger than the polar one, implying thus some significant deformation.

The fast spinning stars with a strong surface magnetic field can be classified into two categories: those for which there are evidences that they are so young that fast rotation together with a strong surface magnetic field is not actually challenging single star models (like σ Ori E) and those for which evidences exist for a sufficiently large age or advanced evolutionary stage that present single star models cannot account for their properties. This second category requires either that the wind magnetic braking law does not apply or that an interaction with a companion spin-up or has (in case of a merging event in a recent past) spin-up the star. Looking at Fig. 8, most of these stars have positions in the HRD compatible with a young age, except HD 345439 where the uncertainties do not allow for drawing a firm conclusion regarding its evolutionary status. In the discussion below, let us keep in mind that the age determinations are obtained from various different modeling assumptions, making this quantity highly uncertain.

HR 7355 (HD 182180) is a helium-strong chemically peculiar star with Balmer emission lines (Rivinius et al. 2008, 2013; Oksala et al. 2010). It shows He-strong absorption and polar field strength between 11 and 12 kG. Its rotation is exceptionally fast with a spin period of 0.52 days (Rivinius et al. 2008; Mikulášek et al. 2010), implying a surface velocity $v_{\text{eq}} = 310 \pm 5$ km s⁻¹ (Rivinius et al. 2013). Mikulášek et al. (2010) estimate the age to be between 15 and 25 Myr and a mass of $6.3 \pm 0.3 M_{\odot}$ using isochrones from Marigo et al. (2008)⁵. Mikulášek et al. (2010) found a characteristic braking timescale of about 0.4 Myr, under the assumption that the star is a solid-body rotator. This short timescale would imply that the star is rapidly undergoing very efficient magnetic braking, suggesting a young age⁶. Thus this would be a challenging case for single star evolution! However, a study by Rivinius et al. (2013) showed that this case might not be so challenging after all when proper account has been made of the gravity darkening effects (see *e.g.* von Zeipel 1924; Espinosa Lara & Rieutord 2011) that are certainly important for such a fast rotating star (see Fig. 2 in Georgy et al. 2014). Rivinius et al. (2013) redetermined the properties of this star accounting for these effects and found a significantly lower mean effective temperature than previously found. From that lower effective temperature, they deduce weaker winds and thus longer magnetic

⁵ Oksala et al. (2010) obtained a gravity $\log g$ equal to 3.95 that would support a younger age for this star.

⁶ Mikulášek et al. (2010) have indeed possibly found evidence for a lengthening of the rotational period with $\dot{P}/P = 2.4(8) \cdot 10^{-6} \text{ yr}^{-1}$ during the last 20 years, *i.e.* 108 ms per year.

wind braking timescale. These authors conclude in contrast with previous works that the age and rapid rotation are not inconsistent with the presence of a fossil magnetic field. This case illustrates the fact that at high rotation, one cannot neglect the effects of the deformation of the star.

According to Grunhut et al. (2012), HR 5907 (or HD 142184 or V1040 Sco) has a spin period of 0.51 day and an equatorial surface velocity of 340 km s^{-1} (Frémat et al. 2005); the star has an effective temperature of $17000 \pm 1000 \text{ K}$, a projected rotational velocity of $290 \pm 10 \text{ km s}^{-1}$, an equatorial radius of $3.1 \pm 0.2 R_{\odot}$ and a stellar mass of $5.5 \pm 0.5 M_{\odot}$, a surface dipole field strength between ~ 10.4 and 15.7 kG . ($V=5.4$, $B2.5V$). It is located in the Upper Scorpius OB association at a distance of $\sim 145 \text{ pc}$ ⁷ (Hernández et al. 2005). Grunhut et al. (2012) also computed the spin-down timescale and found a value of about 8 Myr which is longer than the estimated age of HR 5907 by Hernández et al. (2005), but shorter than the age estimate of 10 Myr by Feiden (2016)⁸ So depending on the age estimate, this star may or may not be a challenging case for single star models.

Two stars HD 345439 and HD 23478 have been discovered serendipitously in the course of the APOGEE (Apache Point Observatory Galactic Evolution Experiment) survey (Eikenberry et al. 2014). They detected the characteristic double-horned profile of emission lines in the Brackett series. This feature comes from material trapped in a magnetosphere rotating rigidly with the star (model of Rigidly Rotating Magnetosphere, RRM, see Townsend & Owocki 2005; Townsend et al. 2010). For HD 345439 these authors deduced from the line profile of He I absorption feature $v \sin i = 270 \pm 20 \text{ km s}^{-1}$. They could not measure from their data the magnetic field, however the presence of a strong magnetic field is made evident through the presence of this RRM. Hubrig et al. (2015), using four subsequent low-resolution FORS 2 spectropolarimetric observation of that star, did not detect any magnetic field at a significance level of 3σ . However this null result may be due to a rapidly varying magnetic field. Analysis of the four individual spectropolarimetric observations of that star is compatible with a variation of about 1 kG of the longitudinal magnetic field in a period of 88 minutes. Its spectral type indicates that it might be a star with a mass similar to σ Ori E. It is difficult to say whether this star poses a challenge in the sense that little is known about its age.

HD 23478 is as HD 345439 a fast rotating star of the σ Ori E type that shows the presence of a rigidly rotating magnetosphere (RRM) (for a detailed study see Sikora et al. 2015). However it is a “He-normal” B3IV star (Eikenberry et al. 2014). A $v \sin i = 125 \pm 20 \text{ km s}^{-1}$ is obtained from the line profile of He I absorption feature⁹. Its sky position and proper motion are compatible with a belonging of that star to the IC 348 young open cluster (proper motions of stars in this cluster have been studied by Scholz et al. 1999). If indeed it is a member of that cluster, then the age of that star would be between 1.3-3 Myr according to Herbig (1998) and between 5-6 Myr according to Bell et al. (2013). Hubrig et al. (2015) performing low-resolution FORS 2 spectropolarimetric observations of that star discovered a rather strong longitudinal magnetic field of up to 1.3-1.5 kG (this is the magnetic field along the line of sight). This star might be an in-

teresting candidate to study in a similar way as σ Ori E. It would be interesting to have data on the braking timescale.

CPD -57°3509 (B2IV) is a member of the Galactic open cluster NGC 3293 that has an age of about 8 Myr (Baume et al. 2003). Przybilla et al. (2016) detected a surface averaged longitudinal magnetic field with a maximum amplitude of about 1 kG. They deduce this star has a bipolar magnetic field with a strength larger than 3.3 kG (assuming a dipolar configuration). They also observe large and fast amplitude variations (within about 1 day) of the longitudinal magnetic field. They interpret this fact as reflecting a very fast rotation (although the projected rotational velocity is small, around 35 km s^{-1}). The star shows no sign of a RRM. They obtain an effective temperature of $23750 \pm 250 \text{ K}$ and a $\log g$ of 4.05 ± 0.10 . Using the Geneva track (Ekström et al. 2012b), they deduce a mass of $9.7 \pm 0.3 M_{\odot}$, a radius of $5.0 \pm 0.9 R_{\odot}$, a $\log L/L_{\odot} = 3.85 \pm 0.13$ and an age of $13.8 + 2.4 - 3.3 \text{ Myr}$. The characteristics deduced from the models by Brott et al. (2011) are respectively $9.2 \pm 0.4 M_{\odot}$, $4.4 + 0.7 - 0.5 R_{\odot}$, $\log L/L_{\odot} = 3.76 \pm 0.12$ and an age of $13.0 + 1.7 - 4.0 \text{ Myr}$. They provide some range for the equatorial velocity between about 70 and 250 km s^{-1} . This star might also be an interesting case for checking the process of wind magnetic braking. An important additional piece of information would be to determine \dot{P} . However, given the high inclination of the star, it seems unlikely we will get \dot{P} any soon.

7. Conclusions and future perspectives

We have revisited here the case of σ Ori E taking benefit from more accurate distance determinations provided by Gaia and a new series of computations that account for both the wind magnetic braking and the magnetic mass loss quenching.

We obtain that σ Ori E is a very young star (age less than 1 Myr) as was obtained by Townsend et al. (2010). The mass of σ Ori E is between 8 and $9 M_{\odot}$ and its metallicity Z (mass fraction of heavy elements) around 0.020. The braking law can well reproduce the observed slowing down in the frame of an aligned dipolar magnetic field topology. We obtain in that case that the polar magnetic field needed is around 14 kG thus two times larger than the observed one. We have not succeeded to resolve this discrepancy. We just noted that the actual magnetic field topology is more complex than a dipolar one and that the present models did not account for any evolution with time of the surface magnetic field. We obtain that the initial rotation of the models fitting σ Ori E is not much constrained and can be anywhere in the range studied here. Because of its very young age, models predict no significant changes of the surface abundances due to rotational mixing for the main isotopes of the CNO elements as well as for helium. This young age remains compatible with an impact of the microscopic diffusion at least in zones stabilized by the surface magnetic field. In regions where low carbon abundance is obtained, it would be very interesting to have nitrogen abundance determinations. If an increase of nitrogen would be found, this would support the view that some material processed by the CN cycle has been brought to the surface.

We see that the knowledge of both the surface velocity and of P/\dot{P} is very constraining and allows to eliminate many models. Also a change in metallicity, typically from 0.014 to 0.020 significantly changes the capacity of the models to provide a good fit. It would be interesting to observe non-magnetic stars in the σ Ori E cluster and to check whether indeed the metallicity is closer to 0.020 rather than 0.014.

It would be interesting to compute models tailored to σ Ori E with different angular momentum transport. For instance,

⁷ The *Gaia* parallaxes confirm this distance for HR 5907, with a parallax of $7.08 \pm 0.14 \text{ mas}$ from DR2 ($141 \pm 3 \text{ pc}$), and $6.990 \pm 0.074 \text{ mas}$ from EDR3 ($143.06 \pm 0.14 \text{ pc}$).

⁸ Actually these authors give age estimates for the Upper Scorpius association to which HR 5907 belongs.

⁹ A previous work obtained a photometric period of 1.0499 days which is slightly faster than the 1.19 days rotation period of σ Ori E (Jerzykiewicz 1993).

if the stars rotate as solid bodies then the surface velocity can be maintained at a higher level everything else kept equal. Indeed solid body rotation implies that the angular momentum is continuously transported from the core to the envelope¹⁰. This implies, at a given age, a higher surface velocity. Now a higher surface velocity also implies a stronger braking mechanism. Thus models need to be computed to study the net effect. In addition, the chemical mixing is significantly changed and this has an impact on the evolutionary tracks, making it difficult to guess what would be the result. This question will deserve a study on its own.

Acknowledgements. The authors thanks the anonymous referee for her/his constructive report that has helped improving the paper. They thank Georges Alecian for providing information on the microscopic diffusion timescales. This work was sponsored by the Swiss National Science Foundation (project number 200020-172505), National Natural Science Foundation of China (grant No. 12173010), Science and technology plan projects of Guizhou province (Grant No. [2018]5781). GM, SE, PE and CG have received funding from the European Research Council (ERC) under the European Union's Horizon 2020 research and innovation programme (grant agreement No 833925, project STAREX). GAW acknowledges support from the Discovery Grants program of the Natural Sciences and Engineering Research Council (NSERC) of Canada. This work has made use of data from the European Space Agency (ESA) mission *Gaia* (<https://www.cosmos.esa.int/gaia>), processed by the *Gaia* Data Processing and Analysis Consortium (DPAC, <https://www.cosmos.esa.int/web/gaia/dpac/consortium>). Funding for the DPAC has been provided by national institutions, in particular the institutions participating in the *Gaia* Multilateral Agreement.

References

- Babcock, H. W. 1947, *ApJ*, 105, 105
- Baume, G., Vázquez, R. A., Carraro, G., & Feinstein, A. 2003, *A&A*, 402, 549
- Béjar, V. J. S., Martín, E. L., Zapatero Osorio, M. R., et al. 2001, *ApJ*, 556, 830
- Bell, C. P. M., Naylor, T., Mayne, N. J., Jeffries, R. D., & Littlefair, S. P. 2013, *MNRAS*, 434, 806
- Brott, I., de Mink, S. E., Cantiello, M., et al. 2011, *A&A*, 530, A115
- Caballero, J. A. 2007, *A&A*, 466, 917
- Caballero, J. A. 2017, *Astronomische Nachrichten*, 338, 629
- Caballero, J. A. 2018, *Research Notes of the American Astronomical Society*, 2, 25
- Cunha, K., Smith, V. V., & Lambert, D. L. 1998, *ApJ*, 493, 195
- de Jager, C., Nieuwenhuijzen, H., & van der Hucht, K. A. 1988, *A&AS*, 72, 281
- Eikenberry, S. S., Chojnowski, S. D., Wisniewski, J., et al. 2014, *ApJ*, 784, L30
- Ekström, S., Georgy, C., Eggenberger, P., et al. 2012a, *A&A*, 537, A146
- Ekström, S., Georgy, C., Granada, A., Wyttenbach, A., & Meynet, G. 2012b, *ASPC*, 453, 353
- Ekström, S., Meynet, G., Maeder, A., & Barblan, F. 2008, *A&A*, 478, 467
- Espinosa Lara, F. & Rieutord, M. 2011, *A&A*, 533, A43
- Feiden, G. A. 2016, *A&A*, 593, A99
- Frémat, Y., Zorec, J., Hubert, A.-M., & Floquet, M. 2005, *A&A*, 440, 305
- Gaia Collaboration, Brown, A. G. A., Vallenari, A., et al. 2018, *A&A*, 616, A1
- Georgy, C., Ekström, S., Eggenberger, P., et al. 2013, *A&A*, 558, A103
- Georgy, C., Granada, A., Ekström, S., et al. 2014, *A&A*, 566, A21
- Georgy, C., Meynet, G., Ekström, S., et al. 2017, *A&A*, 599, L5
- Groote, D. & Hunger, K. 1982, *A&A*, 116, 64
- Grunhut, J. H., Rivinius, T., Wade, G. A., et al. 2012, *MNRAS*, 419, 1610
- Haemmerlé, L., Eggenberger, P., Ekström, S., et al. 2019, *A&A*, 624, A137
- Herbig, G. H. 1998, *ApJ*, 497, 736
- Hernández, J., Calvet, N., Hartmann, L., et al. 2005, *AJ*, 129, 856
- Hubrig, S., Schöller, M., Fossati, L., et al. 2015, *A&A*, 578, L3
- Hunger, K., Heber, U., & Groote, D. 1989, *A&A*, 224, 57
- Jerzykiewicz, M. 1993, *A&AS*, 97, 421
- Keszthelyi, Z., Meynet, G., Shultz, M. E., David-Uraz, A., et al. 2020, *MNRAS*, 493, 518
- Keszthelyi, Z., Meynet, G., Georgy, C., Wade, G. A., Petit, V., & David-Uraz, A. 2019, *MNRAS*, 485, 5843
- Keszthelyi, Z. and Wade, G. A. & Petit, V. 2017, *IAUS*, 329, 250
- Keszthelyi, Z., Meynet, G., Martins, F., de Koter, A., & David-Uraz, A. 2021, *MNRAS*
- Krtićka, J., Mikulášek, Z., Prvák, M., et al. 2020, *MNRAS*, 493, 2140
- Landstreet, J. D. & Borra, E. F. 1978, *ApJ*, 224, L5
- Lindegren, L., Klioner, S. A., Hernández, J., et al. 2020, arXiv e-prints, arXiv:2012.03380
- Luri, X., Brown, A. G. A., Sarro, L. M., et al. 2018, *A&A*, 616, A9
- Marigo, P., Girardi, L., Bressan, A., et al. 2008, *A&A*, 482, 883
- Meynet, G., Eggenberger, P., & Maeder, A. 2011, *A&A*, 525, L11
- Michaud, G. 1970, *ApJ*, 160, 641
- Michaud, G., Alecian, G., & Richer, J. 2015, *Atomic Diffusion in Stars*
- Mikulášek, Z., Krtićka, J., Henry, G. W., et al. 2008, *A&A*, 485, 585
- Mikulášek, Z., Krtićka, J., Henry, G. W., et al. 2010, *A&A*, 511, L7
- Mikulášek, Z., Krtićka, J., Henry, G. W., et al. 2011, *A&A*, 534, L5
- Oksala, M. E., Kochukhov, O., Krtićka, J., et al. 2015, *MNRAS*, 451, 2015
- Oksala, M. E., Wade, G. A., Marcolino, W. L. F., et al. 2010, *MNRAS*, 405, L51
- Oksala, M. E., Wade, G. A., Townsend, R. H. D., et al. 2012, *MNRAS*, 419, 959
- Oliveira, J. M., Jeffries, R. D., Kenyon, M. J., Thompson, S. A., & Naylor, T. 2002, *A&A*, 382, L22
- Osmer, P. S. & Peterson, D. M. 1974, *ApJ*, 187, 117
- Panei, J. A., Vallverdú, R. E., & Cidale, L. S. 2021, *A&A*, 650, A92
- Petit, V., Keszthelyi, Z., MacInnis, R., et al. 2017, *MNRAS*, 466, 1052
- Petit, V., Owocki, S. P., Wade, G. A., et al. 2013, *MNRAS*, 429, 398
- Przybilla, N., Fossati, L., Hubrig, S., et al. 2016, *A&A*, 587, A7
- Reiners, A., Stahl, O., Wolf, B., Kaufer, A., & Rivinius, T. 2000, *A&A*, 363, 585
- Rivinius, T., Tefl, S. Á., Townsend, R. H. D., & Baade, D. 2008, *A&A*, 482, 255
- Rivinius, T., Townsend, R. H. D., Kochukhov, O., et al. 2013, *MNRAS*, 429, 177
- Schaefer, G. H., Hummel, C. A., Gies, D. R., et al. 2016, *AJ*, 152, 213
- Scholz, R.-D., Brunzendorf, J., Ivanov, G., et al. 1999, *A&AS*, 137, 305
- Scott, P., Asplund, M., Grevesse, N., Bergemann, M., & Sauval, A. J. 2015, *A&A*, 573, A26
- Sherry, W. H., Walter, F. M., Wolk, S. J., & Adams, N. R. 2008, *AJ*, 135, 1616
- Shultz, M., Rivinius, T., Das, B., Wade, G. A., & Chandra, P. 2019a, *MNRAS*, 486, 5558
- Shultz, M. E., Owocki, S., Rivinius, T., et al. 2020, *MNRAS*, 499, 5379
- Shultz, M. E., Wade, G. A., Rivinius, T., et al. 2019b, *MNRAS*, 485, 1508
- Sikora, J., Wade, G. A., Bohlender, D. A., et al. 2015, *MNRAS*, 451, 1928
- Stift, M. J. & Alecian, G. 2016, *MNRAS*, 457, 74
- Townsend, R. H. D., Oksala, M. E., Cohen, D. H., Owocki, S. P., & ud-Doula, A. 2010, *ApJ*, 714, L318
- Townsend, R. H. D. & Owocki, S. P. 2005, *MNRAS*, 357, 251
- Townsend, R. H. D., Owocki, S. P., & Groote, D. 2005, *ApJ*, 630, L81
- Townsend, R. H. D., Rivinius, T., Rowe, J. F., et al. 2013, *ApJ*, 769, 33
- ud-Doula, A. & Owocki, S. P. 2002, *ApJ*, 576, 413
- ud-Doula, A., Owocki, S. P., & Townsend, R. H. D. 2009, *MNRAS*, 392, 1022
- Ud-Doula, A., Owocki, S. P., & Townsend, R. H. D. 2009, *MNRAS*, 392, 1022
- von Zeipel, H. 1924, *MNRAS*, 84, 665
- Wolff, S. C. 1968, *PASP*, 80, 281
- Zahn, J.-P. 1992, *A&A*, 265, 115

¹⁰ Local conservation of the angular momentum produces a decrease of the angular velocity in the outer expanding layers and an increase in the contracting core, thus solid body rotation requires to slow down the core and accelerate the envelope.